Nanoscale Advances

ROYAL SOCIETY OF CHEMISTRY

PAPER

View Article Online
View Journal | View Issue

Open Access Article. Published on 24 January 2022. Downloaded on 2/4/2026 12:54:06 PM.
This article is licensed under a Creative Commons Attribution-NonCommercial 3.0 Unported Licence.

Check for updates

Cite this: *Nanoscale Adv.*, 2022, **4**, 1422

Highly porous nitrogen-doped carbon superstructures derived from the intramolecular cyclization-induced crystallization-driven self-assembly of poly(amic acid)†

Hui Sun, *[a] Xiao Li,[a] Kai Jin,[a] Xiaoyong Lai *[a] and Jianzhong Du *[b]

Received 6th December 2021
Accepted 24th January 2022

DOI: 10.1039/d1na00853f

rsc.li/nanoscale-advances

Hierarchically porous carbon nanomaterials have shown significant potential in electrochemical energy storage due to the promoted charge and mass transfer. Herein, a facile template-free method is proposed to prepare nitrogen-doped carbon superstructures (N-CSs) with multi-level pores by pyrolysis of polymeric precursors derived from the intramolecular cyclization-induced crystallization-driven self-assembly (ICI-CDSA) of poly(amic acid) (**PAA**). The excellent thermal stability of **PAA** enables the N-CSs to inherit the hierarchical structure of the precursors during pyrolysis, which facilitates the formation of meso- and macropores while the decomposition of the precursors promotes the creation of micropores. Electrochemical tests demonstrate the ultrahigh surface-area-normalized capacitance (76.5 $\mu F\ cm^{-2}$) of the N-CSs facilitated by the hierarchically porous structure, promoting the charge and mass transfer, as well as the high utilization of pyridinic and pyrrolic nitrogen (12.9%) to provide significant pseudocapacitance contribution up to 40.6%. Considering the diversity of monomers of **PAA**, this ICI-CDSA strategy could be extended to prepare carbon nanomaterials with various morphologies, pore structures and chemical compositions.

Introduction

Porous carbon nanomaterials have drawn wide attention for decades due to their superior stability and excellent physiochemical properties such as high specific surface area and abundant pore structures.[1–5] These outstanding properties make them promising candidates in electrochemical applications including energy storage and electrochemical catalysis.[6–8] Heteroatom doping and adjustment of the pore structure are efficient strategies to improve the electrochemical performance of carbon materials.[9–12] Pores with different diameters have various functions in electrochemical applications. For instance, micropores with diameter less than 2 nm facilitate charge storage when used as an electrode of supercapacitors. Mesopores with diameter between 2 and 50 nm promote the electrolyte transport, leading to the improvement of the reaction rate of electrochemical processes. And macropores serve as the 'ion cell' to provide sufficient electrolyte ions during electrochemical reactions.[13,14]

There are several methods to create pores with different sizes in carbon nanomaterials such as activating by pore forming substrates like KOH and introducing soft or hard templates.[15–17] Self-assembly of amphiphilic polymers is a powerful tool to fabricate functional nanomaterials with diverse morphologies and structures.[18–22] Using polymers with abundant aromatic backbones such as polypyrrole and polyaniline *etc.* as building blocks, carbon nanomaterials with desired structures could be prepared by the pyrolysis of the polymeric precursors obtained.[23–26] Importantly, the structure of the polymeric precursors could be well-preserved during pyrolysis due to the high thermal stability and carbon yield of the precursors.[27–29] Moreover, pores with different sizes could also be created by the pyrolysis of polymeric precursors.[30–35] For instance, Feng and coworkers fabricated flower-like carbon superstructures derived from the hierarchical assembly of polyimide nanosheets. Micropores with sizes of 1.6 and 1.9 nm, and mesopores with a size of 3.9 nm were obtained by the pyrolysis of polymeric precursors and KOH activation.[36] Our group prepared nitrogen-doped hollow carbon spheres using polymer vesicles as the precursor. And the pore size could be controlled within 3.8 to 32.3 nm by cross-linking of the vesicles.[37] Recently, Zhou at al. prepared hollow carbon spheres with uniform micropores (0.5–1.0 nm) and high specific surface area up to 2580 $m^2\ g^{-1}$ using alternating copolymer vesicles as the precursor, followed by KOH activation.[38] However, the self-assembly process is usually

[a]State Key Laboratory of High-Efficiency Coal Utilization and Green Chemical Engineering, Ningxia University, Yinchuan 750021, China. E-mail: sunhui@nxu.edu.cn; xylai@nxu.edu.cn

[b]School of Materials Science and Engineering, Tongji University, Shanghai 201804, China. E-mail: jzdu@tongji.edu.cn

† Electronic supplementary information (ESI) available. See DOI: 10.1039/d1na00853f

© 2022 The Author(s). Published by the Royal Society of Chemistry

Open Access Article. Published on 24 January 2022. Downloaded on 2/4/2026 12:54:06 PM.
This article is licensed under a Creative Commons Attribution-NonCommercial 3.0 Unported Licence.

conducted in dilute solutions, which hinders the scalable fabrication of carbon nanomaterials.

In our previous study, we proposed the new concept of ICI-CDSA, and the self-assembly driving force and mechanism were also investigated.[39] However, the ICI-CDSA was still performed in dilute solution (<4%). In this study, we extended ICI-CDSA to induce the hierarchical self-assembly of **PAA** with a high solid content (15%) and on a large scale (more than 10.0 g), which could be used as a precursor to prepare N-CSs with multi-level pores, as shown in Scheme 1. With the thermal treatment of **PAA**, the solvophobic and crystalline polyimide (PI) segments were introduced into the backbone of the polymer, denoted as P($AA_{0.08}$-*stat*-$I_{0.92}$) (the subscript refers to the percentage of **PAA** and PI segments), leading to the formation of hourglass-shaped superstructures. After calcination in an inert atmosphere, N-CSs with micro-, meso-, macro pores and a high intrinsic nitrogen content of 7.9% were formed, endowing the N-CSs with excellent rate capacity as the electrode material for supercapacitors. Besides, we confirmed that the multi-level pores promoted the utilization of pyridinic nitrogen (N-6) and pyrrolic nitrogen (N-5) of N-CSs, which provided considerable pseudocapacitance contribution.

Experimental section

Materials

Hydrazine hydrate (98%), pyromellitic dianhydride (PMDA, 99%), KBr (99.9%), acetone (AR) and dimethyl formamide (DMF, AR) were purchased from Aladdin. DMSO-d_6 was purchased from J&K Scientific Ltd.

Characterization

The hydrodynamic diameter and polydispersity of the nanostructures and their intermediates were determined using a ZETASIZER Nano series instrument (Malvern Instruments ZS 90) at a scattering angle of 90°. The zeta potentials of the

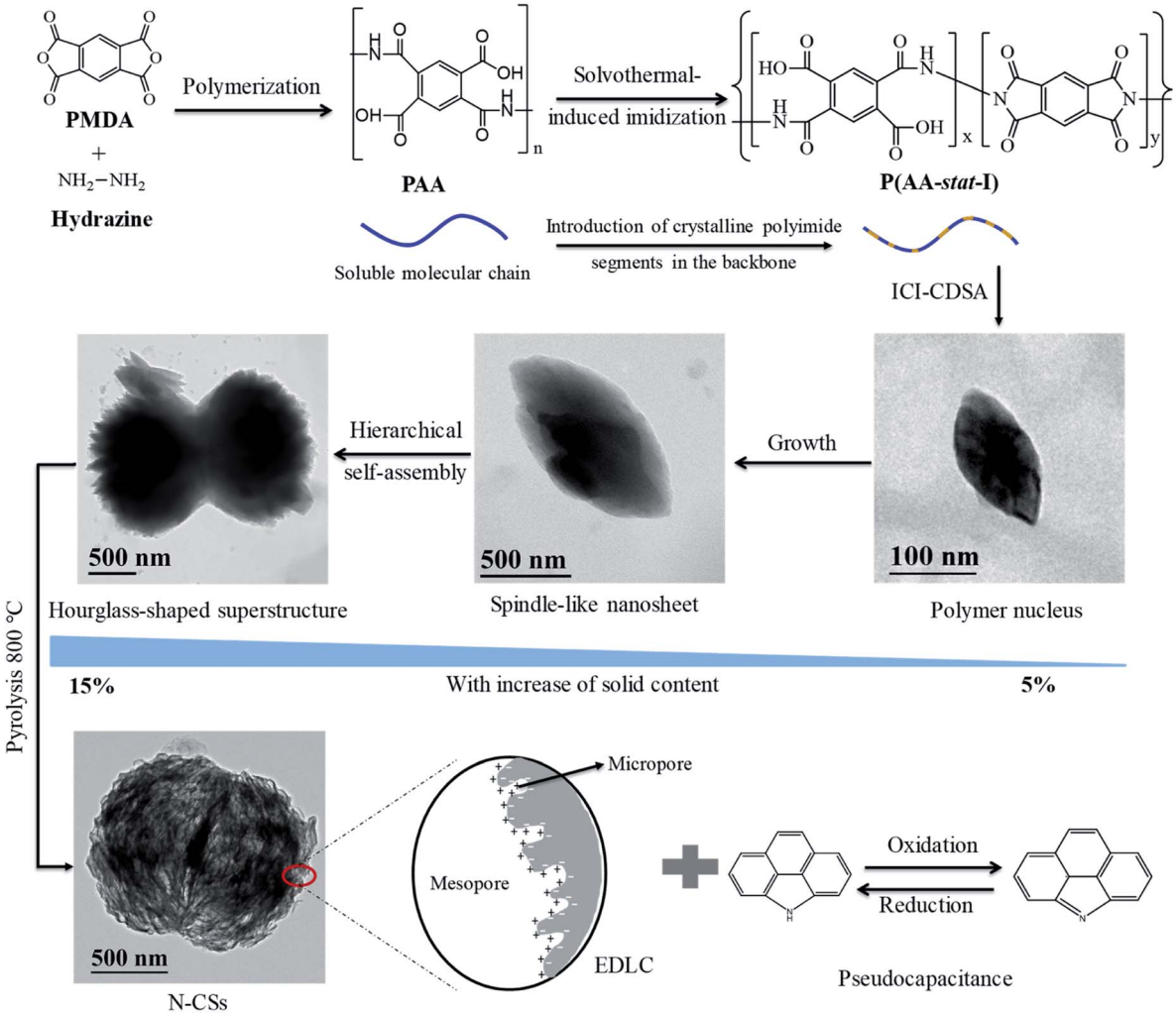

Scheme 1 Synthesis of **PAA** *via* stepwise polymerization and the corresponding thermally induced imidization reaction. With the formation of polyimide segments, spindle-like nanosheets were formed by ICI-CDSA, which further self-assembled to an hourglass-shaped nanostructure at high concentration. The N-CSs with multi-level pores could be obtained by the pyrolysis of the hourglass-shaped precursors at 800 °C. And the schematic illustration of the EDLC and pseudocapacitance of N-CSs.

© 2022 The Author(s). Published by the Royal Society of Chemistry

Open Access Article. Published on 24 January 2022. Downloaded on 2/4/2026 12:54:06 PM. This article is licensed under a Creative Commons Attribution-NonCommercial 3.0 Unported Licence.

samples were also obtained using the same instrument. The transmission electron microscopy (TEM) images were recorded on a JEOL JEM-2100F instrument at 200 kV equipped with a Gatan 894 Ultrascan 1k CCD camera. To obtain scanning electron microscopy (SEM) images, gold nanoparticles were coated on the surface of the samples and they were viewed by using an FEI Quanta 200 FEG electron microscope operated at 10 kV. The X-ray diffraction (XRD) patterns of the samples were obtained using a Bruker D8 ADVANCE X-ray diffractometer. The angle was set from 5° to 50° with a rate of 6° min^{-1}. The Raman spectrum of the N-CSs was recorded by using a LabRAM HR Evolution laser confocal microscopic Raman spectrometer (HORIBA Scientific). Thermogravimetry-differential scanning calorimetry (TG-DSC) was conducted using a DSC Q600 (TA Instruments) with a heating rate of 10 °C min^{-1} to 1000 °C. Nitrogen adsorption/desorption isotherms were measured at −196 °C with a Micromeritics ASAP 2020 instrument. X-ray photoelectron spectroscopy (XPS) spectra were measured using a PHI 5000C ESCA System XPS (PerkinElmer Co., America) with an aluminum target, a voltage of 14.0 kV and power of 300 W.

Synthesis of PAA

PAA was synthesized following our previous study.[39] Generally, hydrazine hydrate (1.139 g, 22.5 mmol) was dissolved in 20 mL of DMF. PMDA (4.867 g, 20.00 mmol) was dispersed in 20 mL of DMF and added into the DMF solution of hydrazine hydrate batch by batch in an hour at 0 °C. Then the solution was stirred for an hour to promote the complete consumption of the monomers.

ICI-CDSA of PAA in DMF

The stock solution of **PAA** was diluted to different concentrations: 50, 75, 100, 125 and 150 mg mL^{-1}, respectively. Then the solutions were heated to 153 °C in an oil bath for 10 min. After cooling to room temperature, the dispersion was centrifuged and washed with water three times. Then the samples were dried under vacuum to give yellow powders.

Preparation of N-CSs

The N-CSs were obtained by the pyrolysis of the polymeric precursor in a nitrogen atmosphere. Typically, 200 mg of polymeric precursor was placed in a tube furnace. After purging nitrogen for 30 min, the tube furnace was allowed to heat to 700, 800 and 900 °C with a rate of 10 °C min^{-1}. The temperature was kept at 800 °C for 2 h and naturally cooled to room temperature, leading to the formation of N-CSs.

Electrochemical measurement

A homogeneous slurry was prepared by mixing 80 wt% of active materials, 10 wt% of acetylene black and 10 wt% of polytetrafluoroethylene (PTFE), which was then pressed onto a nickel foam, serving as the current collector. The electrochemical measurements were conducted using a three-electrode system in 6 M KOH, in which platinum foil serves as the counter electrode and a Hg/HgO electrode serves as the reference electrode. The cyclic voltammetry (CV), galvanostatic charge–discharge (GC) and electrochemical impedance spectroscopy (EIS) measurements were performed using a CHI 660E electrochemical workstation.

Results and discussion

Synthesis and ICI-CDSA of PAA

PAA was synthesized by stepwise polymerization of hydrazine and PMDA following our previous study.[39] The molecular weight, molecular weight distribution and thermally induced imidization process were studied by nuclear magnetic resonance (NMR), gel permeation chromatography (GPC) and real time Fourier transform infrared spectroscopy (RT-FTIR).[39] We have proposed the concept of ICI-CDSA in our previous study.[39] In this study, we focus on the scalable preparation of N-CSs with multi-level pores by a template-free method. The raw solution (solid content of 15%) of **PAA** was heated to 153 °C to induce the intramolecular imidization reaction. The color of the solution turned yellow and the solution became turbid, indicating the formation of nanostructures. It is noteworthy that the ICI-CDSA of **PAA** could be performed on a large scale (more than 10.0 g) by a one-pot synthesis, as shown in the digital photo in Fig. 1A. Powder XRD was used to verify the crystal structure of the nano-objects, which crystallized in the monoclinic spacegroup, as shown in Fig. 1B. The strong intensity of the isolated peaks demonstrated the high crystallinity of the nano-objects, in accordance with our previous result.[39] The diffraction peaks of (002), (110) and (200) planes were located at 2θ of 10.2, 18.3 and 29.2°, corresponding to the *d*-spacing of 0.87, 0.48 and 0.31 nm respectively.

The morphology of the nano-object was revealed by TEM and SEM. As shown in Fig. 1C–E, the TEM images revealed the hourglass-shaped structure of the nano-objects. Besides, the TEM image in Fig. 1E disclosed the microstructure of the hourglass-shaped superstructure, and overlapped triangular spines were observed on the surface. Then SEM was also conducted to observe the surface morphology of the hourglass-shaped superstructure, as shown in Fig. 1F and G. It was clearly observed that the hourglass-shaped superstructure was formed by spindle-like nanosheets, as pointed by the overlapped nanosheets in the red circle in Fig. 1D. Furthermore, nano-objects with various morphologies could be prepared by ICI-CDSA under different conditions, as illustrated in Fig. S1.†

Formation mechanism of hourglass-shaped superstructures

To reveal the formation mechanism of hourglass-shaped superstructures, the self-assembly process was investigated, as shown in Fig. 2. The P($AA_{0.08}$-*stat*-$I_{0.92}$) underwent a nucleation-growth-hierarchical self-assembly process with the increase of concentration. When the concentration was 50 mg mL^{-1}, the P($AA_{0.08}$-*stat*-$I_{0.92}$) crystallized from DMF to form a spindle-like crystal nucleus (Fig. 2A). As the concentration increased to 75 and 100 mg mL^{-1}, the P($AA_{0.08}$-*stat*-$I_{0.92}$) chains crystallized onto the spindle-like nucleus to form large sized spindle-like

 © 2022 The Author(s). Published by the Royal Society of Chemistry

Open Access Article. Published on 24 January 2022. Downloaded on 2/4/2026 12:54:06 PM.
This article is licensed under a Creative Commons Attribution-NonCommercial 3.0 Unported Licence.

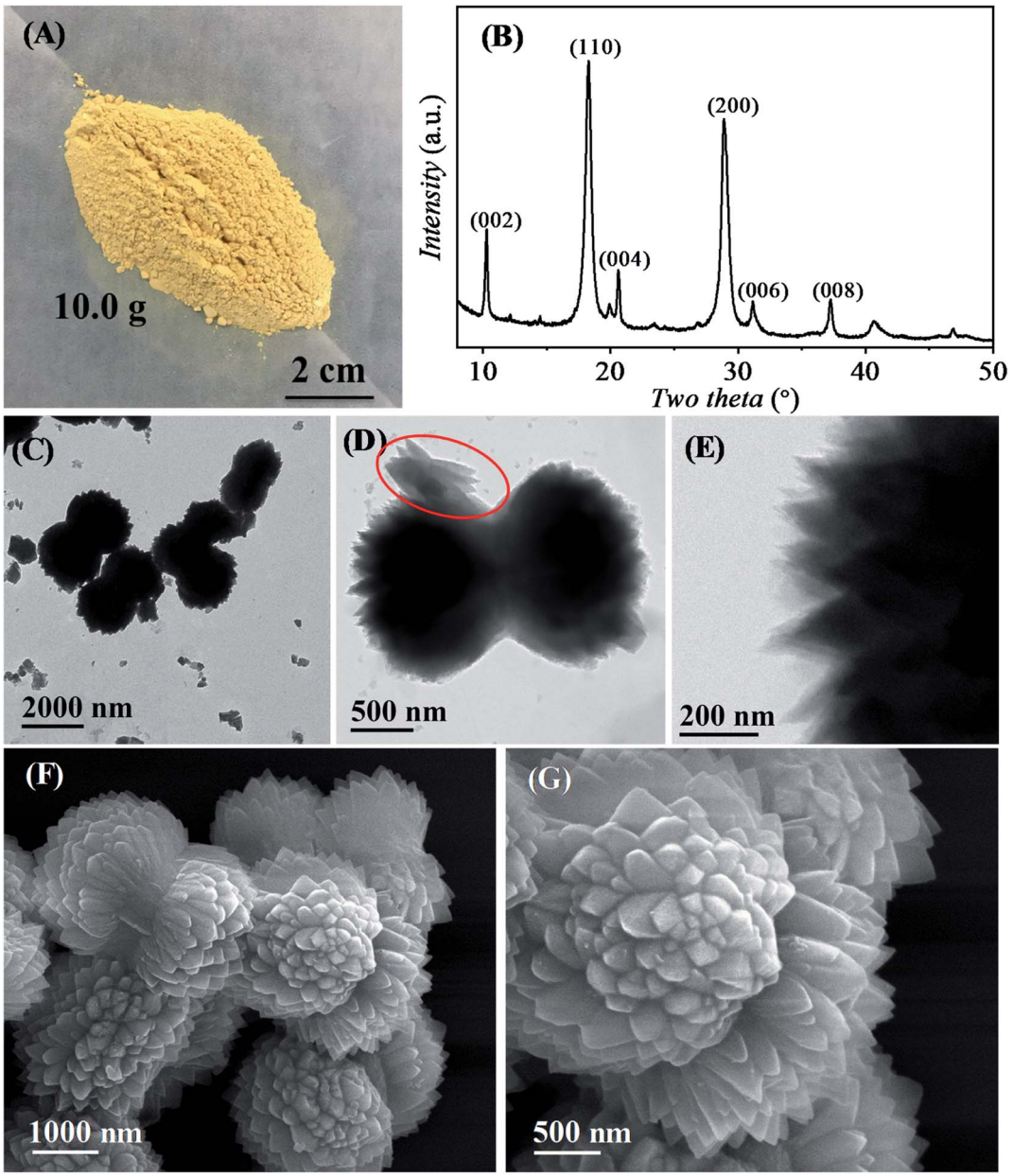

Fig. 1 Hourglass-shaped superstructures prepared by the ICI-CDSA of **PAA**. (A) Digital photo, (B) XRD pattern, (C–E) TEM images and (F), (G) SEM images of hourglass-shaped superstructures.

nanosheets, as illustrated in Fig. 2B–D. When the concentration further increased to 125 mg mL^{-1}, the spindle-like nanosheets underwent hierarchical self-assembly to form bundles of nanosheets (Fig. 2E and F), and eventually hourglass-shaped superstructures (Fig. 1). The corresponding dynamic light scattering (DLS) and zeta potential results are presented in Fig. S2 and S3,† indicating that the size of the nanostructures increased from 603 to 2530 nm with the concentration. However the zeta potentials were maintained at around −20 mV, demonstrating that the unreacted carboxyl groups covered the surface of the nanostructures to prevent agglomeration. In addition, the spindle-like nanosheets pointed by red circles in Fig. 2E and 1D confirmed that the hourglass-shaped superstructures were indeed formed by the hierarchical self-assembly of the spindle-like nanosheets.

N-CSs derived from the pyrolysis of hourglass-shaped superstructures

It has been reported that **PAA** or PI based polymeric nanostructures were promising precursors to prepare carbon nanomaterials with high specific surface area and tunable pore distribution due to their high thermal stability and pyrolysis properties.[36,37,40] The pyrolysis process of the hourglass-shaped superstructure was monitored by TG-DSC, as illustrated in Fig. S4.† There are four stages during calcination in the TG spectrum in Fig. S4B,† (I) removal of free water; (II) occurrence

Open Access Article. Published on 24 January 2022. Downloaded on 2/4/2026 12:54:06 PM.
This article is licensed under a Creative Commons Attribution-NonCommercial 3.0 Unported Licence.

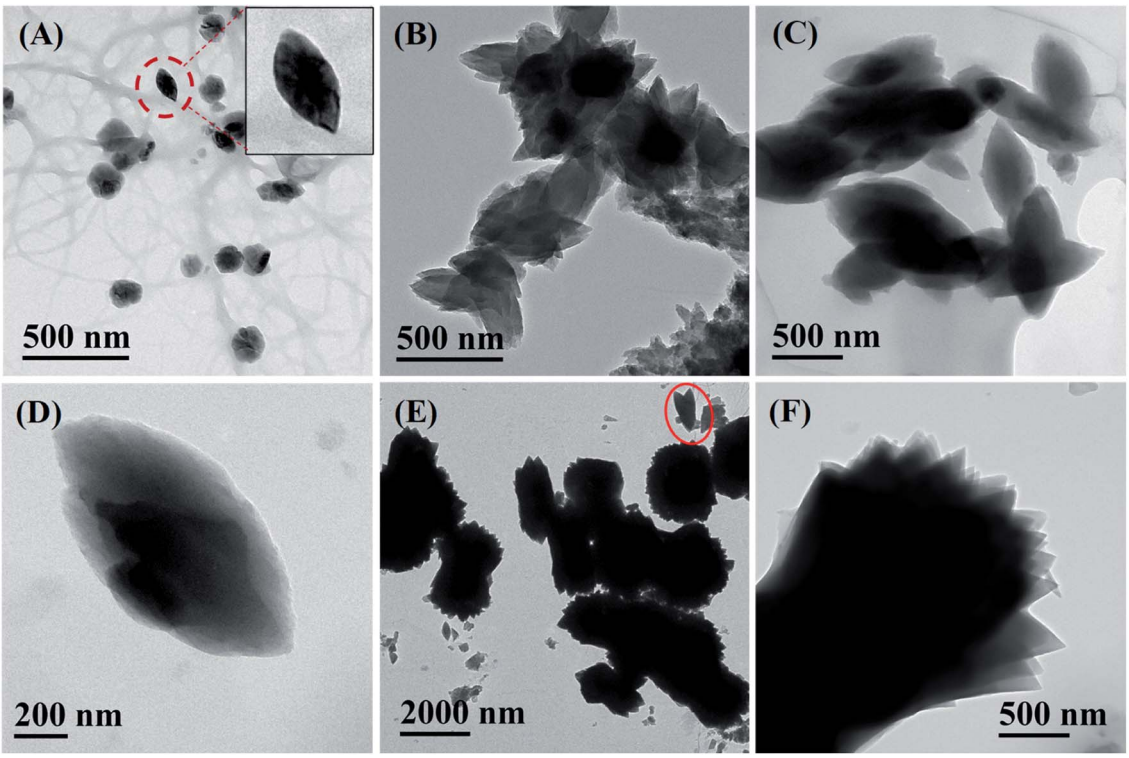

Fig. 2 Monitoring the formation process of the hourglass-shaped superstructures at different concentrations in DMF by TEM. (A) 50, (B) 75, (C and D) 100 and (E and F) 125 mg mL^{-1}. The nanosheets in the red circle in (E) are spindle-like nanosheets.

of the imidation reaction; (III) carbonation process and (IV) further carbonation and decomposition of the carbon skeleton, respectively, as discussed in our previous study.[37]

As shown in Fig. 3, N-CSs composed of carbon nanosheets were obtained after pyrolysis of the hourglass-shaped polymeric precursor in an inert atmosphere, and more SEM images are provided in Fig. S5.† The formation of the sheet-like structure of N-CSs was due to the pyrolysis of the spindle-like nanosheets, which decomposed to small sized nanosheets, as illustrated in Fig. 3A–C. The average thickness of the sheets was measured to be 11.7 ± 0.8 nm, as pointed by the red dash circle in Fig. 3C. The N-CSs pyrolyzed at 700 and 900 °C were also observed by SEM, as shown in Fig. S6.† The morphology of the N-CSs was similar to that obtained at 800 °C. However, we could observe that the pores were not well-developed when the pyrolysis temperature is 700 °C. TEM images in Fig. 3D–F further confirmed the hierarchical porous structure of the N-CSs. It was observed that the nanosheets formed interconnected carbon networks with multi-level pores. Moreover, the supplementary SEM images in Fig. S7† clearly showed the highly porous inner structure of N-CSs. Besides, the high resolution TEM image in Fig. 3G indicated the formation of the graphitic structure during calcination. The amorphous parts in Fig. 3G might be the pores of N-CSs.

The graphitic structure of the N-CSs was further confirmed by Raman and XRD analysis (Fig. 3H and S8†). The separation of the G band and D band as well as the relatively high intensity of the G band (I_G/I_D = 1.03) demonstrated the high degree of graphitization of N-CSs.[41,42] The diffraction peaks centred at 26°and 44° were assigned to the (002) and (101) peaks of graphitic carbon (Fig. S8†).[43,44] The I_G/I_D of N-CSs was 0.85 and 1.03 when the pyrolysis temperature was 700 and 900 °C, respectively (Fig. S9†), revealing the effect of pyrolysis temperature on the degree of graphitization. The low I_G/I_D value of N-CSs pyrolyzed at 700 °C was due to the high nitrogen content (11.9%), which induced the generation of defects of carbon layers. The Brunauer–Emmett–Teller (BET) specific surface area was 380.7 $m^2\ g^{-1}$, as measured by nitrogen adsorption/desorption experiment (Fig. 3I), which is much higher than that of the polymeric precursor (Fig. S10†). Besides, the micropore surface area was 121 $m^2\ g^{-1}$ and the total pore volume was calculated to be 0.69 $cm^3\ g^{-1}$.

Multi-level pores including micropores, small-, medium- and large-sized mesopores were formed after pyrolysis, as shown in Fig. 3J. The pore diameters were centred at 1.0, 3.8, 7.1–11.4 and 12.0–38.6 nm, respectively. We thought that the multi-level pore structure was due to the decomposition and hierarchical structure of the polymeric precursor. With the pyrolysis of the polymer and release of produced gases, micropores with a diameter of 1.0 nm and small-sized mesopores with a diameter of 3.8 nm were formed, which has also been reported previously.[37,45] It could be clearly observed from TEM and SEM images in Fig. 3A–F and S7† that there were mesopores with different sizes inside the N-CSs formed by the loose arrangement of the nanosheets. Besides, there were also large through holes, as indicated by TEM and SEM images in Fig. 3E and S7,†

© 2022 The Author(s). Published by the Royal Society of Chemistry

Open Access Article. Published on 24 January 2022. Downloaded on 2/4/2026 12:54:06 PM.
This article is licensed under a Creative Commons Attribution-NonCommercial 3.0 Unported Licence.

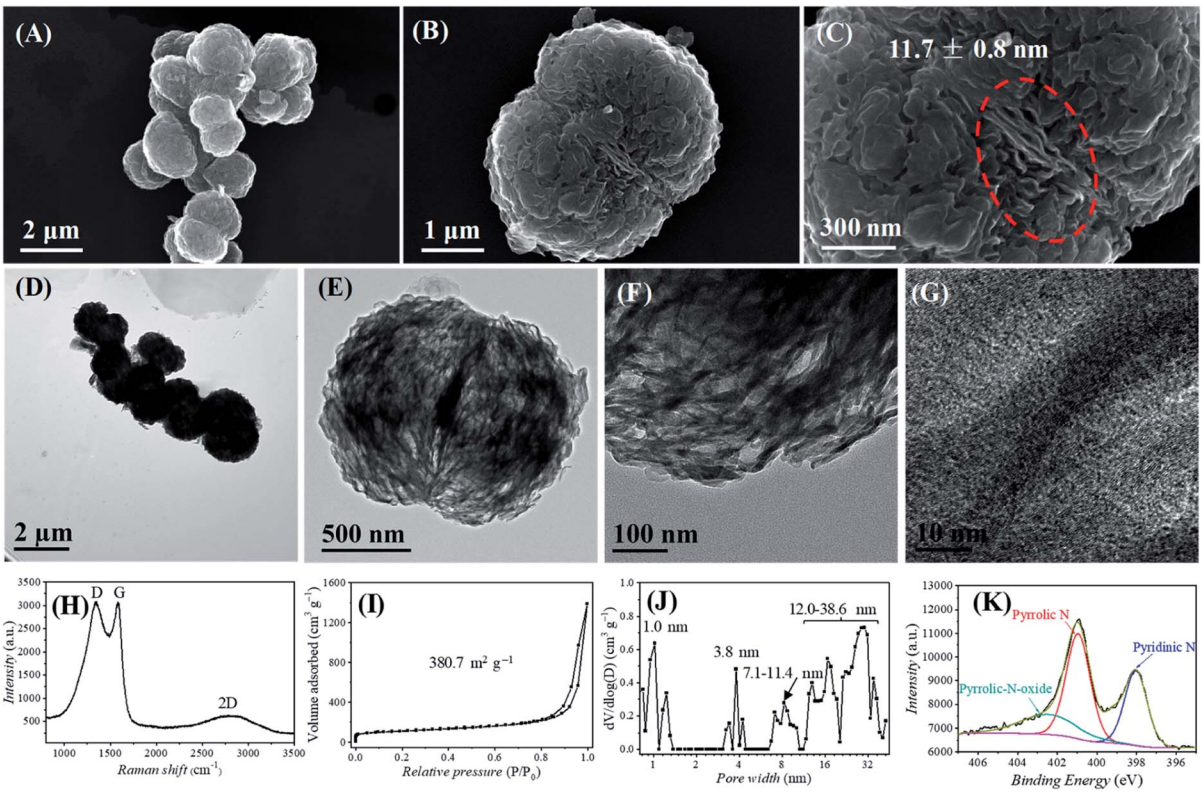

Fig. 3 N-CSs derived from the pyrolysis of hourglass-shaped superstructures in a nitrogen atmosphere. (A–C) SEM and (D–F) TEM images at different magnifications; (G) high resolution TEM image; (H) Raman spectrum; (I) nitrogen adsorption/desorption isotherm; (J) pore distribution and (K) high resolution XPS spectrum of N-CSs.

respectively, which facilitated the mass transport in electrochemical applications, such as electrocatalysis and energy storage.

The elemental composition of the N-CSs was analysed by both elemental analysis and XPS. The elemental analysis gave a composition of 82.5% carbon, 9.6% oxygen and 7.9% nitrogen, respectively, which was consistent with XPS results, as shown in Fig. S11A.† When the pyrolysis temperature increased to 900 °C, the nitrogen content of N-CSs decreased to 4.3%. The high resolution C 1s XPS spectrum illustrated in Fig. S11B† could be fitted with three peaks, corresponding to the sp^2 hybridized graphitic carbon species, C=N bond and C–O bond, respectively.[46,47] It is noteworthy that the intrinsic nitrogen content was as high as 8.1%, as obtained by XPS, which was much higher than that of many nitrogen-doped carbon materials.[1,10,48] The high nitrogen content can improve the wettability of the carbon materials, which benefits the sufficient utilization of the high specific surface area.[49,50] The high resolution N 1s spectrum could be subdivided into three peaks, assigned to pyridinic N, pyrrolic N and pyrrolic-*N*-oxide, respectively. The contents of pyridinic N, pyrrolic N and pyrrolic-*N*-oxide were calculated to be 27.6%, 41.6% and 30.8%, respectively, as shown in Fig. 3K, equivalent to the atomic content of 2.18% and 3.29% of pyridinic N and pyrrolic N. We speculated that the generation of such a high content of active nitrogen species was due to the unique molecular structure of the polymer, which afforded large amount of nitrogen-containing heterocycles in the backbone. Furthermore, the pyridinic N and pyrrolic N are believed to be the active species to supply considerable pseudocapacitance for supercapacitors.[51–54] Upon charging and discharging, redox reactions occurred between active nitrogen species and their counterparts, which enhanced the charge storage capability apart from EDLC, leading to the enhanced specific capacitance.

Electrochemical performance of N-CSs

Taking advantage of the multi-level porous structure and high intrinsic nitrogen content, the N-CSs were used as the active electrode material for supercapacitors. As illustrated in Fig. S12,† the CV curves of N-CSs maintained a quasi-rectangular shape within the scan rates from 2 to 100 mV s^{-1}, demonstrating the excellent high-rate stability.[55] The GC curves in Fig. 4A exhibited the symmetric process of charge and discharge at current densities from 0.5 to 50 A g^{-1}, indicating the outstanding capacitive characteristics and reversibility. The specific capacitance at different current densities was 279.4, 263.7, 253.4, 241.5, 236.8, 235.5 and 233.8 F g^{-1} at current densities of 0.5, 1, 2, 5, 10, 20 and 50 A g^{-1}, respectively, calculated from the discharge curves in Fig. 4A, which was much better than that of N-CSs pyrolyzed at 700 (175.8 F g^{-1}) and 900 °C (186.3 F g^{-1}) due to the well-developed porous structure and high nitrogen content (Fig. S13†). Though the

Open Access Article. Published on 24 January 2022. Downloaded on 2/4/2026 12:54:06 PM.
This article is licensed under a Creative Commons Attribution-NonCommercial 3.0 Unported Licence.

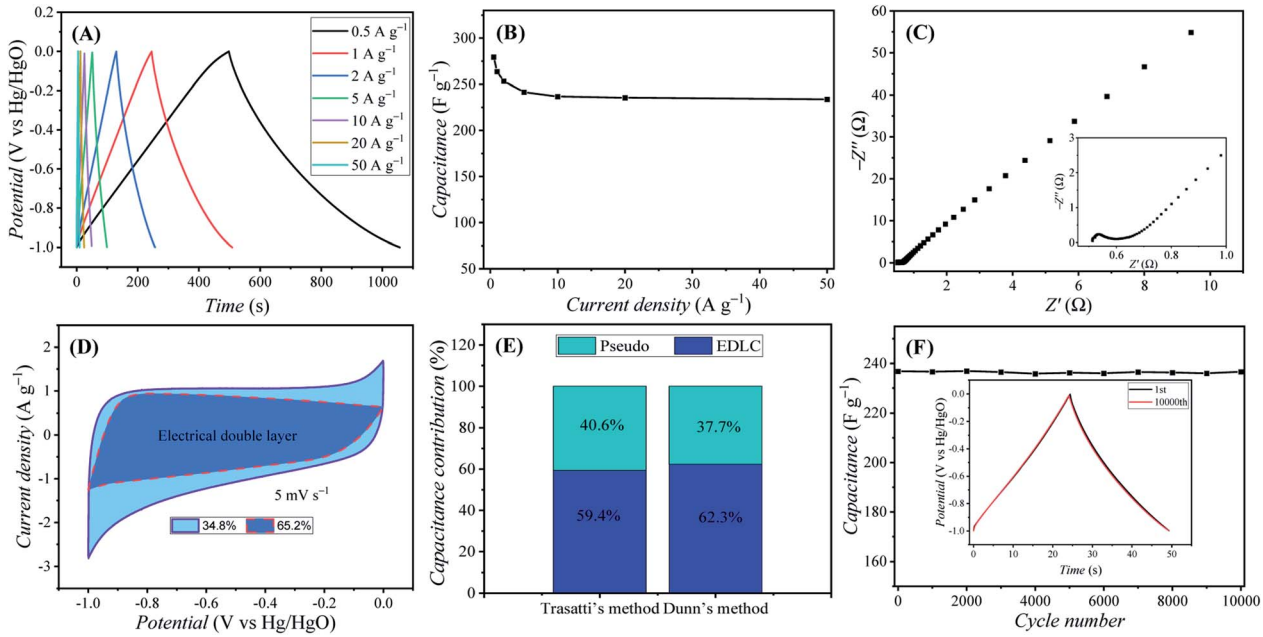

Fig. 4 Electrochemical results and analysis of the N-CSs. (A) GC curves at different current densities, (B) specific capacitance at different current densities, (C) EIS spectrum; the inset shows the enlarged EIS spectrum at high frequencies (D) capacitance contribution of electrical double layer capacitive (EDLC, navy blue) and pseudocapacitive (light blue) processes at 5 mV s^{-1} calculated by Dunn's method, (E) comparison of capacitance contribution from the EDLC and pseudo (pseudocapacitance) calculated by Trasatti's and Dunn's methods, and (F) cycle stability of N-CSs at 10 A g^{-1}; the inset shows the CV curves at the first and 10 000th cycles.

high nitrogen doping content could induce defects and increase the electrolyte wettability of N-CSs, the specific capacitance of N-CSs pyrolyzed at 700 °C was pretty low, which might be ascribed to the poor conductivity and not well-developed porous structure. As shown in Fig. 4B, the specific capacitance dropped dramatically when the current density increased from 0.5 to 10 A g^{-1}, and then levelled off at high current densities (20 and 50 A g^{-1}). The specific capacitance at 50 A g^{-1} was still as high as 233.8 F g^{-1}, corresponding to a capacitance retention of 83.7%, which was much better than most of the previous studies.[13,36,37,55] We believed that the high specific capacitance at large current density benefitted from the hierarchically porous structure of the N-CSs, which facilitated the charge storage by micropores, electrolyte transportation by mesopores and electrolyte storage by macropores. Fig. 4C shows the EIS spectrum of the N-CSs. The Nyquist plots showed depressed semicircles with very small radius at high frequencies, indicating the small charge transfer resistance. However the curve at low frequencies with the slope much greater than 1 demonstrated an ideal capacitive behavior and a fast diffusion of the electrolyte ions in the multi-level pores of electrode materials.

Pseudocapacitance is an important contribution to the total capacitance of nitrogen-doped carbon materials in supercapacitors, which can significantly improve the performance of capacitors. Therefore, we evaluated the pseudocapacitance of N-CSs by calculating the surface-area-normalized capacitance (C_A). The C_A of N-CSs was calculated to be 76.5 μF cm^{-2}, much higher than the theoretical EDLC of activated carbon (15–25 μF cm^{-2}) and previously reported carbon materials, as shown in Table S1.†[56] Considering the high content of pyridinic N (N-6, 2.18%) and pyrrolic N (N-5, 3.29%) of N-CSs, we investigated the pseudocapacitance contribution quantitatively by Trasatti's and Dunn's methods. The detailed analysis process is presented in the ESI.†

As shown in Fig. 4D, the EDLC and pseudocapacitance contributions were calculated to be 65.2% and 34.8% at 5 mV s^{-1} by Dunn's method, respectively. The relationship between the EDLC contribution and the square root of the scan rate ($v^{0.5}$) could be well described by linear fitting, as illustrated in Fig. S14.† The EDLC contribution decreased with the slowdown of the scan rate. When the scan rate approached zero, the maximum contribution of pseudocapacitance was obtained (37.7%) due to the sufficient faradaic redox reactions by N-6 and N-5 (Fig. S14†). The contribution of pseudocapacitance of N-CSs could also be regarded as produced by the defects induced by high nitrogen doping. In addition, the contributions of EDLC and pseudocapacitance were also calculated by Trasatti's method, as presented in Fig. S15† and 4E. The pseudocapacitance contribution was calculated to be 40.6%, corresponding to a utilization of 12.9% of N-6 and N-5, as calculated in the ESI,† which is much higher than previous study.[55] The enhanced electrochemical performance of N-CSs was believed to be contributed by the synergy of the highly porous layered structure and high content of active nitrogen species. We believed that the hierarchically porous structure of N-CSs facilitated the sufficient exposure of N-6 and N-5, promoting the faradaic redox reaction and increasing the pseudocapacitance contribution. In addition, negligible specific capacitance attenuation was observed after 10 000 cycles (Fig. 4F), demonstrating the excellent cycle stability of the N-CSs.

© 2022 The Author(s). Published by the Royal Society of Chemistry

Open Access Article. Published on 24 January 2022. Downloaded on 2/4/2026 12:54:06 PM. This article is licensed under a Creative Commons Attribution-NonCommercial 3.0 Unported Licence.

Conclusions

In summary, N-CSs with multi-level pores were prepared by the pyrolysis of hourglass-shaped polymeric precursors derived from the ICI-CDSA of **PAA**. Electrochemical measurements revealed the excellent energy storage capability of the N-CSs. In addition, we investigated the contribution of EDLC and pseudocapacitance to the total capacitance, and the pseudocapacitance contribution reached 40.6%, corresponding to a high utilization of N-6 and N-5 up to 12.9%. The multi-level porous structure of N-CSs was believed to facilitate the electron transfer and ion diffusion during the charge/discharge process, promoting the utilization of active nitrogen species and the contribution of pseudocapacitance.

Author contributions

Conceptualization and supervision: H. S. and J. D. Investigation, resources, methodology, and validation: X. L. and K. J. Writing – original draft: H. S. Writing – review & editing: H. S., X. L. and J. D.

Conflicts of interest

There are no conflicts to declare.

Acknowledgements

This work was supported by Natural Science Foundation of Ningxia (2020AAC03003 and 2021AAC03026). J. D. is a recipient of National Science Fund for Distinguished Young Scholars (21925505). H. S. thanks the Ningxia Youth Talent Support Project of Science and Technology and Young Scholars of Western China of CAS.

Notes and references

1 J. Yang, Z. Ju, Y. Jiang, Z. Xing, B. Xi, J. Feng and S. Xiong, *Adv. Mater.*, 2018, **30**, 1700104.
2 W. Meng, X. Bai, B. Wang, Z. Liu, S. Lu and B. Yang, *Energy Environ. Mater.*, 2019, **2**, 172–192.
3 C.-T. Toh, H. Zhang, J. Lin, A. S. Mayorov, Y.-P. Wang, C. M. Orofeo, D. B. Ferry, H. Andersen, N. Kakenov, Z. Guo, I. H. Abidi, H. Sims, K. Suenaga, S. T. Pantelides and B. Özyilmaz, *Nature*, 2020, **577**, 199–203.
4 L. Peng, H. Peng, C.-T. Hung, D. Guo, L. Duan, B. Ma, L. Liu, W. Li and D. Zhao, *Chem*, 2021, **7**, 1020–1032.
5 X. Zhao, X. Kong, F. Wang, R. Fang and Y. Li, *Angew. Chem., Int. Ed.*, 2021, **60**, 10842–10849.
6 Q. G. Wang, L. He, L. Y. Zhao, R. S. Liu, W. P. Zhang and A. H. Lu, *Adv. Funct. Mater.*, 2020, **30**, 1906117.
7 M. X. Chen, M. Zhu, M. Zuo, S. Q. Chu, J. Zhang, Y. Wu, H. W. Liang and X. Feng, *Angew. Chem., Int. Ed.*, 2019, **58**, 2–9.
8 C. Cui, Y. Gao, J. Li, C. Yang, M. Liu, H. Jin, Z. Xia, L. Dai, Y. Lei, J. Wang and S. Wang, *Angew. Chem., Int. Ed.*, 2020, **59**, 7928–7933.
9 J. Guo, D. Li, Z. Qian, H. Luo, M. Yang, Q. Wang, J. Xu and N. Zhao, *Adv. Funct. Mater.*, 2020, **30**, 1909877.
10 C. Chen, X. Sun, X. Yan, Y. Wu, H. Liu, Q. Zhu, B. B. A. Bediako and B. Han, *Angew. Chem., Int. Ed.*, 2020, **59**, 11123–11129.
11 Q. Lai, J. Zheng, Z. Tang, D. Bi, J. Zhao and Y. Liang, *Angew. Chem., Int. Ed.*, 2020, **59**, 11999–12006.
12 L. Ye, Y. Ying, D. Sun, Z. Zhang, L. Fei, Z. Wen, J. Qiao and H. Huang, *Angew. Chem., Int. Ed.*, 2019, **58**, 3270–3277.
13 W. Tian, H. Zhang, X. Duan, H. Sun, G. Shao and S. Wang, *Adv. Funct. Mater.*, 2020, **30**, 1909265.
14 J. Hwang, A. Ejsmont, R. Freund, J. Goscianska, B. Schmidt and S. Wuttke, *Chem. Soc. Rev.*, 2020, **49**, 3348–3422.
15 S. Kim, M. Ju, J. Lee, J. Hwang and J. Lee, *J. Am. Chem. Soc.*, 2020, **142**, 9250–9257.
16 C. C. Hou, L. Zou and Q. Xu, *Adv. Mater.*, 2019, **31**, e1904689.
17 C. Zhou, C. Lai, D. Huang, G. Zeng, C. Zhang, M. Cheng, L. Hu, J. Wan, W. Xiong, M. Wen, X. Wen and L. Qin, *Appl. Catal., B*, 2018, **220**, 202–210.
18 C. H. Evers, J. A. Luiken, P. G. Bolhuis and W. K. Kegel, *Nature*, 2016, **534**, 364–368.
19 H. Deng, L. Lin, S. Wang, G. Yu, Z. Zhou, Y. Liu, G. Niu, J. Song and X. Chen, *Adv. Mater.*, 2019, **31**, e1903443.
20 Y. Zou, X. Zhou, Y. Zhu, X. Cheng, D. Zhao and Y. Deng, *Acc. Chem. Res.*, 2019, **52**, 714–725.
21 C. Sun, L. Yue, Q. Cheng, Z. Wang and R. Wang, *ACS Mater. Lett.*, 2020, **2**, 266–271.
22 X. Lin, Z. Wang, R. Liu, S. Liu, K. Leng, H. Lou, Y. Du, B. Zheng, R. Fu and D. Wu, *Chem. Commun.*, 2021, **57**, 1446–1449.
23 J. M. Serrano, T. Liu, A. U. Khan, B. Botset, B. J. Stovall, Z. Xu, D. Guo, K. Cao, X. Hao, S. Cheng and G. Liu, *Chem. Mater.*, 2019, **31**, 8898–8907.
24 W. Song, Y. Zhang, A. Varyambath and I. Kim, *ACS Nano*, 2019, **13**, 11753–11769.
25 J. Wei, Z. Sun, W. Luo, Y. Li, A. A. Elzatahry, A. M. Al-Enizi, Y. Deng and D. Zhao, *J. Am. Chem. Soc.*, 2017, **139**, 1706–1713.
26 T. Zhao, A. Elzatahry, X. Li and D. Zhao, *Nat. Rev. Mater.*, 2019, **4**, 775–791.
27 D. Kim, A. Kirakosyan and J. Choi, *Macromol. Rapid Commun.*, 2016, **37**, 1507–1512.
28 Z. Zhou and G. Liu, *Small*, 2017, **13**, 1603107.
29 K. W. Tan and U. Wiesner, *Macromolecules*, 2019, **52**, 395–409.
30 D. Li, L.-X. Ding, H. Chen, S. Wang, Z. Li, M. Zhu and H. Wang, *J. Mater. Chem. A*, 2014, **2**, 16617–16622.
31 J. Zhang, D. Yang, W. Li, Y. Gao and H. Li, *Electrochim. Acta*, 2014, **130**, 699–706.
32 D. Liu, G. Cheng, H. Zhao, C. Zeng, D. Qu, L. Xiao, H. Tang, Z. Deng, Y. Li and B.-L. Su, *Nano Energy*, 2016, **22**, 255–268.
33 Y. Chang, C. Yuan, C. Liu, J. Mao, Y. Li, H. Wu, Y. Wu, Y. Xu, B. Zeng and L. Dai, *J. Power Sources*, 2017, **365**, 354–361.
34 J. Liu, N. P. Wickramaratne, S. Z. Qiao and M. Jaroniec, *Nat. Mater.*, 2015, **14**, 763–774.
35 S. Dutta, A. Bhaumik and K. C. W. Wu, *Energy Environ. Sci.*, 2014, **7**, 3574–3592.

© 2022 The Author(s). Published by the Royal Society of Chemistry

Open Access Article. Published on 24 January 2022. Downloaded on 2/4/2026 12:54:06 PM.
This article is licensed under a Creative Commons Attribution-NonCommercial 3.0 Unported Licence.

36 Z. Xu, X. Zhuang, C. Yang, J. Cao, Z. Yao, Y. Tang, J. Jiang, D. Wu and X. Feng, *Adv. Mater.*, 2016, **28**, 1981–1987.
37 H. Sun, Y. Q. Zhu, B. Yang, Y. F. Wang, Y. P. Wu and J. Z. Du, *J. Mater. Chem. A*, 2016, **4**, 12088–12097.
38 C. Li, T. Rasheed, H. Tian, P. Huang, Y. Mai, W. Huang and Y. Zhou, *ACS Macro Lett.*, 2019, **8**, 331–336.
39 H. Sun and J. Du, *Macromolecules*, 2020, **53**, 11033–11039.
40 Z. Wang, H. Ogata, S. Morimoto, M. Fujishige, K. Takeuchi, Y. Hashimoto and M. Endo, *Carbon*, 2014, **72**, 421–424.
41 Y. Sun, R. B. Sills, X. Hu, Z. W. Seh, X. Xiao, H. Xu, W. Luo, H. Jin, Y. Xin, T. Li, Z. Zhang, J. Zhou, W. Cai, Y. Huang and Y. Cui, *Nano Lett.*, 2015, **15**, 3899–3906.
42 L. Miao, D. Zhu, M. Liu, H. Duan, Z. Wang, Y. Lv, W. Xiong, Q. Zhu, L. Li, X. Chai and L. Gan, *Chem. Eng. J.*, 2018, **347**, 233–242.
43 J. Liang, Z. Xiao, Y. Gao, X. Xu, D. Kong, M. Wagner and L. Zhi, *Carbon*, 2019, **143**, 487–493.
44 M. Yang, X. Long, H. Li, H. Chen and P. Liu, *ACS Sustainable Chem. Eng.*, 2019, **7**, 2236–2244.
45 Z. Xu, D. Lu, L. Ma, C. Lu, X. Xi, G. Zhang, R. Liu and D. Wu, *Chem. Eng. J.*, 2019, **364**, 201–207.
46 Z.-L. Yu, G.-C. Li, N. Fechler, N. Yang, Z.-Y. Ma, X. Wang, M. Antonietti and S.-H. Yu, *Angew. Chem., Int. Ed.*, 2016, **55**, 14623–14627.
47 F. Böttger-Hiller, P. Kempe, G. Cox, A. Panchenko, N. Janssen, A. Petzold, T. Thurn-Albrecht, L. Borchardt, M. Rose and S. Kaskel, *Angew. Chem., Int. Ed.*, 2013, **52**, 6088–6091.
48 C. Zhang, J. Liu, Y. Ye, Q. Chen and C. Liang, *Carbon*, 2020, **156**, 31–37.
49 C. Pu, J. Zhang, G. Chang, Y. Xiao, X. Ma, J. Wu, T. Luo, K. Huang, S. Ke, J. Li and X. Yang, *Carbon*, 2020, **159**, 451–460.
50 S. Zhu, X. Dong, H. Huang and M. Qi, *J. Power Sources*, 2020, **459**, 228104.
51 Z. Xie, X. Shang, J. Yang, B. Hu, P. Nie, W. Jiang and J. Liu, *Carbon*, 2020, **158**, 184–192.
52 Q. Jia, C. Yang, Q. Pan, Y. Xin, F. Xu, W. Qi, H. Wei, S. Yang, C. Zhou, N. Hu and B. Cao, *Chem. Eng. J.*, 2020, **383**, 123153.
53 K. Gong, F. Du, Z. Xia, M. Durstock and L. Dai, *Science*, 2009, **323**, 760–764.
54 D. Guo, R. Shibuya, C. Akiba, S. Saji, T. Kondo and J. Nakamura, *Science*, 2016, **351**, 361–365.
55 L. Zhang, T. Wang, T.-N. Gao, H. Xiong, R. Zhang, Z. Liu, S. Song, S. Dai and Z.-A. Qiao, *CCS Chem.*, 2020, **2**, 870–881.
56 Z. Li, L. Zhang, B. S. Amirkhiz, X. Tan, Z. Xu, H. Wang, B. C. Olsen, C. M. B. Holt and D. Mitlin, *Adv. Energy Mater.*, 2012, **2**, 431–437.

© 2022 The Author(s). Published by the Royal Society of Chemistry